

1 **Deformation controlled Long-Period seismicity in low cohesion volcanic sediments**

2

3

4

Pete Rowley^{1,2}, Philip P Benson¹, Christopher J Bean³

5

6

¹ Rock Mechanics Laboratory, School of Earth and Environmental Sciences, University of Portsmouth,
7 Portsmouth, PO1 3QL, UK

7

8

² Department of Geography and Environmental Management, Frenchay Campus, UWE, Bristol,
9 Coldharbour Lane, Bristol BS16 1QY, UK

9

10

³ Geophysics Section, Dublin Institute for Advanced Studies, School of Cosmic Physics, 5 Merrion Square,
11 Dublin 2, Ireland

11

12 **Abstract**

13 Volcano seismicity is an important tool in remotely monitoring and forecasting activity at volcanoes
14 around the world. Volcanic earthquakes show diverse spectral characteristics, with shallow Long Period
15 (Low Frequency) seismicity and long duration tremor generally interpreted as indicators of fluid
16 migration, and as potential precursors to eruption. Here we show that a common low-cohesion volcanic
17 sediment from Campi Flegrei caldera (Italy) produces Low Frequency and long duration seismicity whilst
18 undergoing deformation in dry conditions. We employ acoustic-emission rock deformation experiments
19 at a range of strain rates to produce events which are spectrally indistinguishable when normalised for
20 scale from Long Period and tremor seismicity observed in natural volcanic settings. Generation of these
21 signals is enhanced at lower strain rates. Correlated X-Ray tomography of samples before and after
22 deformation constrain the source as distributed damage.

23 Given the ubiquitous nature of slow edifice deformation, and the frequent occurrence of such low
24 cohesion materials in the upper edifice of volcanoes, we suggest low frequency seismicity and tremor in
25 volcanic settings do not require fluid movement. Instead, these characteristic signals can be an indicator
26 that deformation within the edifice is being accommodated by weak volcanoclastic materials.

27 **Introduction**

28 Volcano seismic monitoring is a key component of hazard management at volcanic centres around the
29 world, enabling centralized observatory staff to monitor otherwise remote volcanoes. This is important
30 as the increase in event-rate and character of seismic activity is strongly correlated with increasing
31 volcanic rest and ultimately to eruption¹⁻³. However, any hazard warning process is dependent on the
32 quality of data gathered, and on the interpretation of that data in understanding volcanic processes.

33 A number of diagnostic volcanoseismic signals have identified as occurring within the near-surface
34 volcanic edifice⁴, and are used in forecasting the eruption potential of active volcanoes. Long period (LP)
35 and seismic tremor events are thought to be a result of fluid oscillation or movement within the volcanic
36 edifice^{2,5,6}, and are characterized by long trains of low frequency signals lasting seconds (LP) to days
37 (tremor). They often have no clear onset which makes 3D location difficult. Volcano-tectonic (VT) events
38 are rapid-onset broad spectrum events, associated with rock fracture, as with tectonic events⁷. Hybrid
39 earthquakes display the rapid and high frequency onset of VT events, with a subsequent low frequency
40 train similar to LP events, and are usually interpreted as a combination of new fracture formation
41 followed by fluid movement⁸.

42 Of these, LP events and seismic tremor have been used as key early warning indicators, as the inference
43 that fluid is moving may indicate either magma progression through the edifice, or movement of newly
44 heated groundwater. However, despite the desire of scientists to use the fluid-related data to better
45 forecast unrest, this has proved difficult. An improved understanding of the cause of these signals would
46 enable better interpretation of seismic monitoring for improved hazard assessment, as false alarm
47 evacuations can have disproportionate socioeconomic impacts on communities⁹⁻¹³, while missed
48 evacuations may directly result in unnecessary fatalities¹⁴. An increasingly recognised issue is that
49 volcanic areas consist of a wide variety rocks, spanning from competent lavas to poorly consolidated ash
50 and pumice. These latter rock type scatter and corrupt seismic energy in ways that are not fully
51 understood from a rock physics perspective^{15,16}.

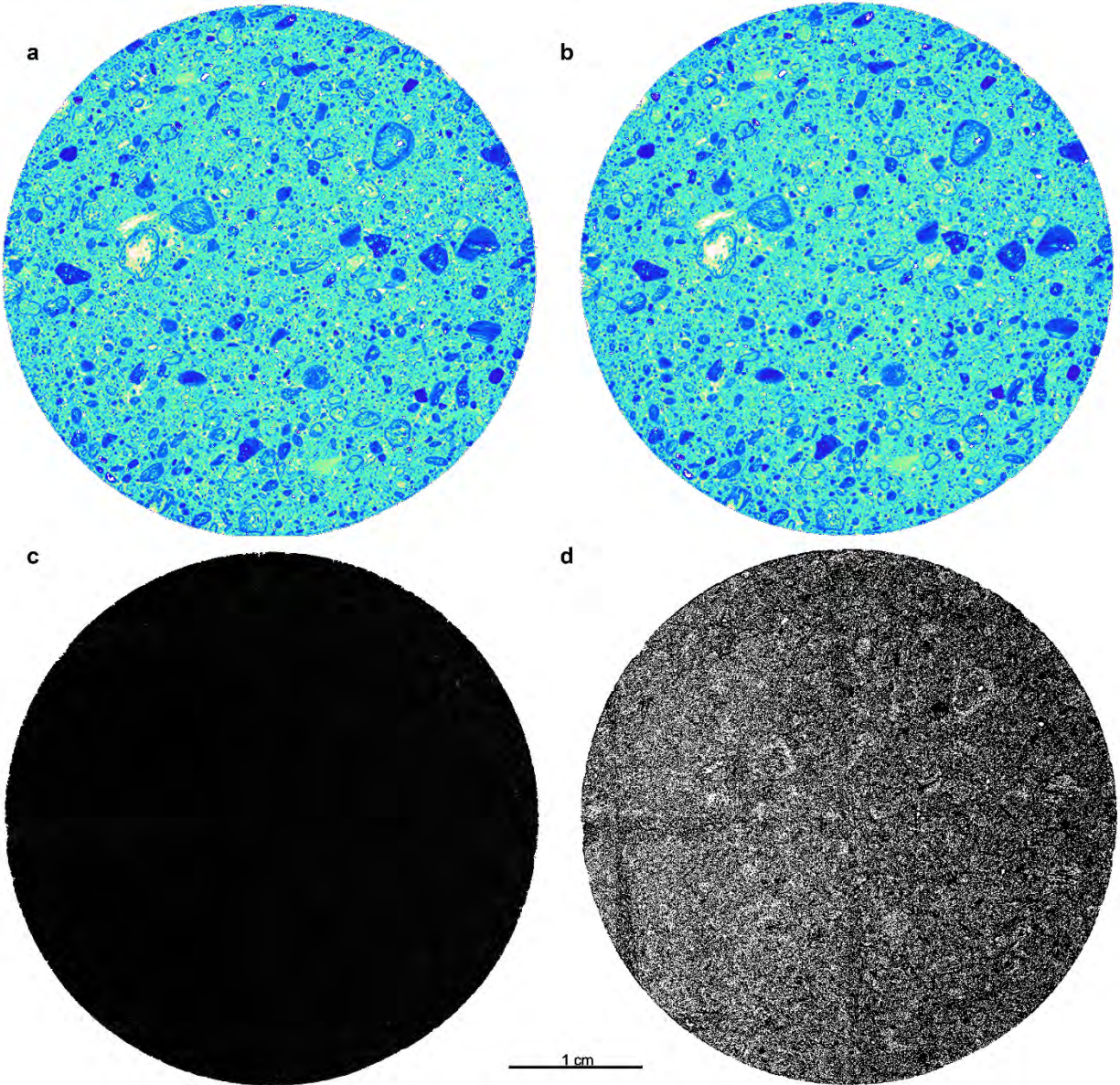
52 To better understand these LF and seismic tremor data, we here report a laboratory study using
53 Neapolitan Yellow Tuff (NYT), as a representative example of the types of a weak volcanoclastic sediment
54 often found within volcanic architectures. The NYT is a 40 km³, often massive lapilli tuff, erupted from
55 Campi Flegrei 14.9±0.4 ka^{13,17,18}, and therefore also forms part of the sedimentary cover involved in
56 ongoing volcanic deformation in the area^{19–21}. Produced during what is believed to be a
57 phraeatomagmatic eruption, it is rich in pumice and pumiceous ash, with some lithics, and occasional
58 accretionary lapilli²². The tuff as a whole is greater than 80 m thick in places, with the deposits showing
59 intermittent dune bedforms and cross stratification as well as the more typical massive form. Its
60 strength is low enough to be broadly representative of weakly lithified volcanic sediments in the upper
61 edifice of active volcanoes around the world^{23–25}.

62 To better understand fluid-rock processes in the volcanic plumbing system, which may not be easily
63 accessed in the field, considerable effort has been made to develop laboratory experiments with which
64 to simulate volcano-tectonic pressures²⁶ and temperatures²⁷. By combining high pore pressure fluid (and
65 fluid movement) with freshly faulted rock samples, the seismic signature of the coupled rock-fluid has
66 been simulated. The analogue of tectonic earthquakes is recorded on the cm-scale using an array of
67 Acoustic Emission (AE) sensors, which have a relatively flat response across 100-800 kHz to capture
68 seismicity at the laboratory scale^{5,28}. Importantly, the physics of fracture and seismicity follows classical
69 Boltzmann statistics allowing event sequences and character to be considered scale invariant, and
70 allowing the AE at micrometre scale to be robustly applied to seismicity at kilometre scale^{29,30}. Recent
71 work has shown that the ratio of the scale of the feature (fault, conduit) to the seismicity follow a
72 constant^{5,31,32}, and have successfully been used to model seismic processes in volcanic settings^{33,34}.

73 **Mechanical behaviour**

74 The NYT is a weak material, and – for the blocks used in this work – we find unconfined compressive
75 strength (UCS) of dried samples in the range of 6-8MPa (consistent with previous work³⁵). This places it
76 at the weaker end of volcanoclastic sediments which have been tested²⁵. We measure a cohesion of 0.18
77 MPa, comparable with that of medium clays, but far lower than that of either typical crystalline volcanic
78 rocks (e.g. Columbia Plateau Basalt, 1-4 MPa) or more lithified ignimbrite material (Calico Hills tuff, 1.7-
79 4.4 MPa). We therefore consider that the NYT is an appropriate analogue for the weak volcanoclastic
80 sediments found in the upper edifice of volcanoes, while retaining the competence necessary to
81 undergo coring and testing.

82 The nature of deformation during these experiments is dependent on strain rate. High strain rate
83 conditions generate noticeable fractures running through the sample, with lengths on the order of
84 centimetres, while low strain rate deformation results in shortening with no evidence of macroscopic
85 fracture. This observation is supported by the use of X-ray computed tomography (XCT) analysis of the
86 cores before and after deformation. Comparing virtual slices of the pre-and post-deformation cores
87 reveals no visible fracturing or localised deformation at the resolution of the imaging (Figure 1). Given
88 the 2% shortening of each sample during deformation this indicates that the damage was diffuse. Given
89 the XCT resolution of 20 µm and the lack of individual damage zones, we are restricted to saying that the
90 length scale of motion for individual AE events is no more than this resolution, and quite likely
91 substantially smaller.



92

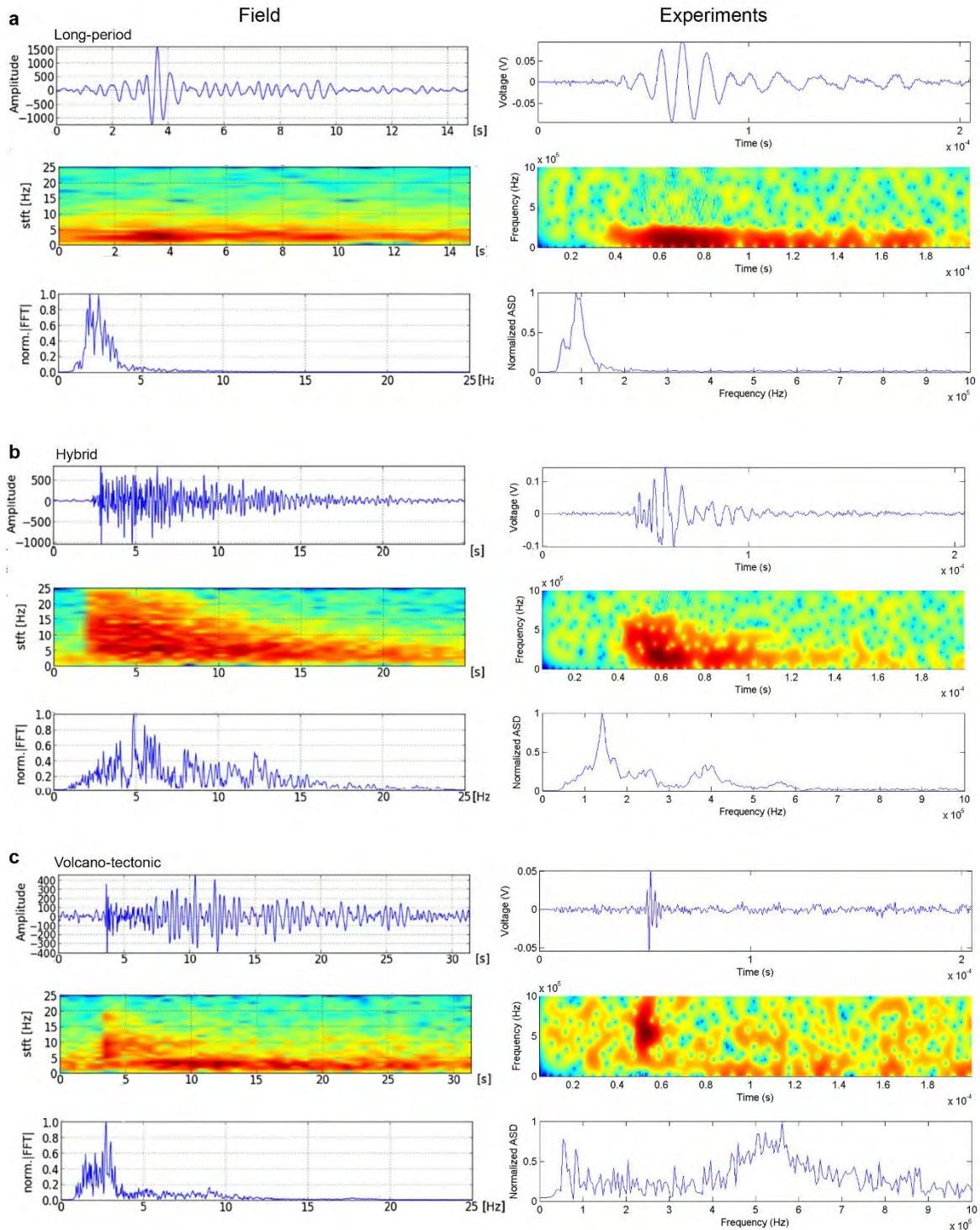
93 Figure 1. Example X-Ray computed tomography virtual slices of a sample before and after a low strain
 94 rate deformation experiment. **a** False-coloured section before testing, and **b** matched location after
 95 testing. **c** A comparison between pixel values in slices **a** and **b**, with bright pixels representing more
 96 difference on a grayscale range from 0 (black) to 255 (white). The dark colour indicates a broadly
 97 unchanged pixel character across the entire slice. **d** A high contrast version of **c**, stretching the grayscale
 98 across only the lowest 8 values. This threshold analysis shows that what little difference is present is
 99 localised around grain boundaries. This difference approach will preferentially highlight boundaries
 100 between material types, suggesting the deformation is even more diffuse than this analysis indicates. At
 101 this level of exaggeration weak linear artefacts are visible running vertically and horizontally across the
 102 image as a result of the XCT imaging process.

103

104 On the macro-scale, it is notable that there is no obvious 'barrelling' of the samples, whereby axial
105 shortening is accompanied by lateral extension due to cataclasis and flow in the materials, as is common
106 in lower porosity materials. The exceptionally high porosity and therefore space accommodation
107 potential of the material is likely to account for this lack of radial strain in the samples. Post-experiment,
108 all specimens were recovered from the rubber jacket without collapsing, maintaining structural
109 integrity. This mode of failure is similar to that seen in compaction bands³⁶, rather than a propagating
110 brittle failure via shear zones as commonly generated in competent (strong) rocks³⁷.

111 **Spectral character of microseismicity in the Neapolitan Yellow Tuff**

112 Acoustic emission was recorded during deformation of each sample in order to characterise the seismic
113 behaviour under different conditions. Experiments using oven-dried samples, under both high and low
114 strain rates ($1 \times 10^{-5} \text{ s}^{-1}$ & $4 \times 10^{-6} \text{ s}^{-1}$ respectively), produced spectra with dominant frequencies in the
115 ranges 100 kHz to 150 kHz, and bimodal split across peaks at 150kHz and 600kHz. These are qualitatively
116 very similar to the spectral features of volcanic LP, tremor, and hybrid type signals (Figure 2). Fracture
117 propagation in competent, high cohesion rocks^{33,38-40} is usually dominated by broad spectrum, short
118 duration (10^{-5} s) events with spectral similarity to classic tectonic and volcano-tectonic (VT) seismic
119 signatures (spectra covering the 200-800 kHz band and durations of $<10^{-5} \text{ s}$, e.g. Fig 2a), as reported
120 from deformation of basalt^{33,34,41}. It is therefore notable that the NYT is almost completely dominated by
121 activity in the low frequency (0-350 kHz) band, with durations into 10^{-4} and 10^{-3} s . Moreover, whilst LP
122 data has been postulated to rely on fluid movement driving conduit/crack resonance to generate a
123 lower frequency harmonic^{5,42}, here the samples are dry and so this generation mechanism is not
124 available.



125

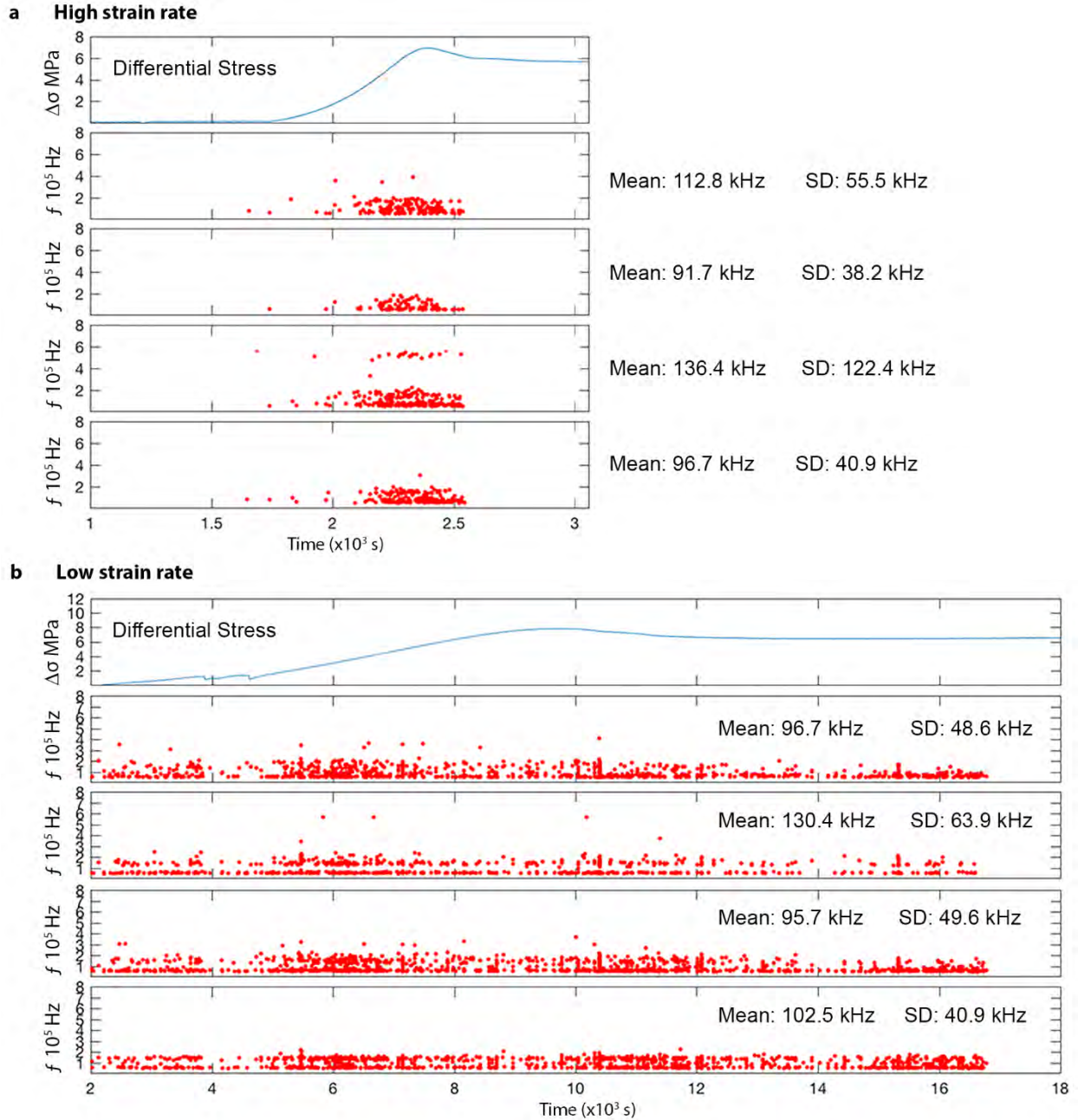
126 Figure 2 - Event representations of typical natural volcanic events⁴ and typical experimental events
 127 recorded in this work, representing **a** long period (LP), **b** hybrid and **c** volcano tectonic (VT) style
 128 seismicity. Each event shows the vertical component of the velocity seismogram (or voltage for the
 129 experimental equivalent, which is proportional to magnitude of compression), Fourier spectrogram, and
 130 normalized Fourier transform.

131

132 The different event types have particular spectral characters; The LP/ tremor-like events (Fig 2a) show
133 peak amplitudes at between 50 and 150 kHz with narrow spectra containing little signal above 400 kHz.
134 These signals can have durations exceeding 1×10^{-3} s. Hybrid events (Figure 1b) have a broad-band
135 initial response, between 50 and 700 kHz, which gradually and sequentially loses the higher frequency
136 components until the signal dies out completely, after approximately 1×10^{-4} s. The VT-like events
137 (Figure 2c) have a broad band emission across the sensor range (50 kHz – 800 kHz), although often with
138 an emphasised peak amplitude between 400-700 kHz. They have durations in the realm of 1×10^{-5} s.
139 Note that real field events can look more complex in detail, often due to wave scattering at
140 heterogeneous edifice structures.

141 **Strain-rate dependent emission character**

142 We explore the low frequency dominance in these experiments using average peak FFT, extracted from
143 the continuously logged 10 MHz data stream (Figure 3). High strain rate experiments have a different AE
144 behaviour to slow strain rate conditions. The brittle failure at high strain rates is accompanied by
145 accelerating AE (Figure 3a), including VT, LP and hybrid-like signals. This continues throughout the ~10
146 minute window as the differential stress climbs from zero, through the elastic-deformation phase, to the
147 peak strength of the material. However, after the sample passes its peak strength and deformation goes
148 into strain-weakening behaviour the AE stops. We interpret this as a localisation of deformation along
149 the coherent fracture planes which have formed, lubricated by gouge.



150

151 Figure 3 - Differential stress and moving average peak FFT frequency through time for 4 of the 12 AE
 152 channels in **a** high strain rate and **b** low strain rate experimental conditions. Note different horizontal
 153 scales. High strain rate experiments show accelerating AE until brittle failure of the sample. Low strain
 154 rate experiments show continuous activity throughout deformation.

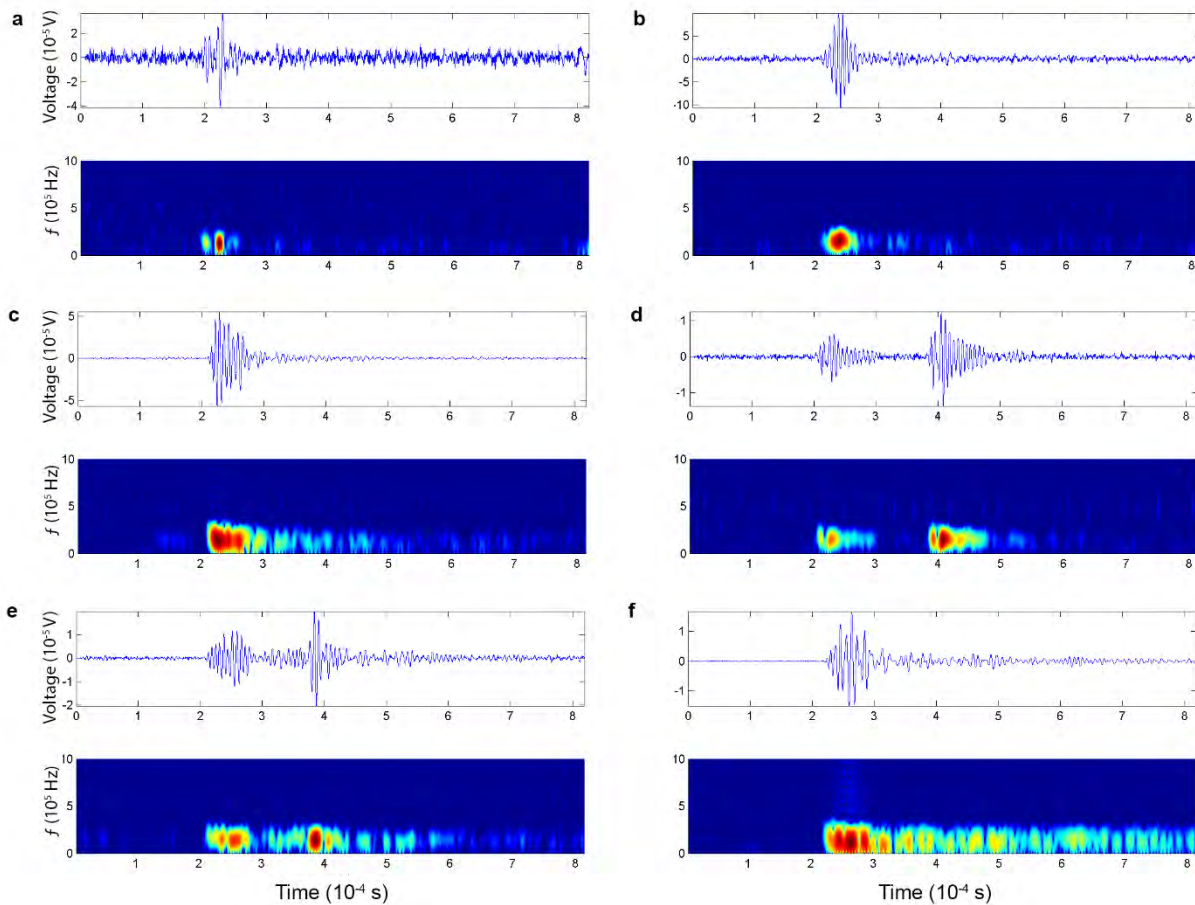
155

156 In contrast, the low strain rate experiment (Fig 3b) begins exhibiting relatively consistent 'tremor-like'
 157 AE from the start of deformation, and throughout the experiment for over 5 hours, with evidence of
 158 slightly more activity in the first half of the elastic deformation phase, and in the strain weakening phase
 159 before the material behaves in a ductile manner. FFT analysis of these events allows moving average

160 peak amplitude frequencies to be extracted, which give values of 119 kHz for the fast condition (σ 16.0
 161 kHz) and 102 kHz for the slow strain rate condition (σ 15.3 kHz). This suggests that while both
 162 experiments are being dominated by low frequency LP and tremor-like signals the faster strain rate has
 163 a higher proportion of higher frequency VT- and hybrid-like signals. This is consistent with samples of
 164 individual event spectrograms generated for each experiment, which suggest in high strain rate
 165 experiments that $\sim 7.5\%$ of the signals are hybrid-like, and $\sim 1\%$ VT-like, whereas in low strain rate
 166 conditions under 1% of the AE are either VT- or hybrid-like. The remaining events are constrained
 167 entirely in the low frequency band (< 350 kHz).

168 **Generation of low frequency signal**

169 While the LP- and tremor-like signals have very characteristic spectra, and they can be observed
 170 exhibiting durations two orders of magnitude longer than the VT-like events, there is a notable
 171 recurrence of events with similar durations to VT events but constrained to the LP- and tremor-like
 172 frequency band. High resolution AE spectrograms (Figure 4) suggest that many LP- and tremor-like
 173 signals may in fact be comprised of individual short-duration or overlapping events, sometimes
 174 exhibiting long trains of decreasing amplitude, sometimes with no clear train, and others with the trains
 175 punctuated by new peaks in activity at the same frequency.



176
 177 Figure 4 – **a-f** varied LP-type activity, which can be single or multiple pulse, with event timescales varying
 178 from 1×10^{-5} s to 1×10^{-3} s.

179

180 This rich behaviour seen in the experimental data shows a good qualitative match with field
181 observations. The short duration pulses seen throughout the signals in Figure 4 bear similarity to pulse-
182 like LP events⁴³, and to the often observed close relationship between LP and tremor, where rapidly
183 repeating LPs have been seen to merge into longer duration tremor signals⁴⁴. The detail of this character
184 is seen in Figure 4f, where short duration LP events are embedded within low amplitude continuous
185 tremor-like signals.

186

187 **Discussion**

188 Low cohesion volcanoclastic sediment has a substantially different acoustic emission behaviour to more
189 common geomaterials which have been investigated in the laboratory to date, with a predominance of
190 low frequency, long duration events. The propensity for the NYT to generate LP-like signals dominates
191 the spectral characteristics regardless of strain rate under the conditions tested. Whilst VT-like events
192 do occur, they represent a minority of the signal, as demonstrated by the mean FFTs (Figure 3).

193 Earthquake dominant frequencies scale with source dimension³¹, so we use the established approach³²
194 $d_1 \times f_1 = d_2 \times f_2$ where d and f are the dimension and frequency of the events in the experiments (1)
195 and the field (2) to explore the agreement between field and experiment. Spectral data for f_1 and f_2
196 (Figure 2) gives values for f_2/f_1 in the order of 10^5 . Using XCT to assess damage in the tested material
197 we find that d_1 has values *less than* 2×10^{-5} m, with this being a maximum value limited by the resolution
198 of the XCT (Figure 1). This limits the length of rupture deformation in the field to <1 m, emitting at ~ 1
199 Hz). More likely, the deformation we see in the core is being accommodated by damage at smaller
200 scales below the XCT resolution, bringing the associated anticipated deformation at volcanoes into the
201 cm-scale seen commonly in active volcanic systems⁴⁵.

202 It has been suggested that shallow LP signals, and by inference, seismic tremor, may be generated by
203 slow-failure in low strength materials⁴³. The experiments here support the interpretation that
204 deformation in dry materials can generate these signals. Using cross-correlated XCT images, we have, for
205 the first time, been able to infer sub-grain scale distributed intergranular deformation of low cohesion
206 sediments, linked to low frequency sustained acoustic emission. This suggests that LP seismicity may be
207 generated distributed damage in low-cohesion materials accompanying edifice deformation.

208 Furthermore, these results suggest that deformation within weak porous volcanic materials may trigger
209 similar signals to tremor and LP seismicity at low confining pressures, but without the presence or
210 interaction of fluids. Given the frequent observation of shallow ground deformation in volcanic settings,
211 it seems likely the conditions for subjecting volcanic sediments to these types of conditions are
212 widespread. We do not suggest that tremor and LP signals cannot be produced by hydrothermal fluid
213 and magma migration, but we highlight a mechanism for shallow seismicity and tremor unrelated to
214 magma movement, with the capacity to confound the current interpretation of volcanic LP seismicity as
215 always fluid-derived.

216 **Method**

217 The Neapolitan Yellow Tuff (Campi Flegrei, Italy) was collected from the Liccarblock quarry
218 (40°53'29.42"N, 14° 6'25.74"E). Its physical characteristics were constrained using a range of uniaxial,
219 triaxial shear tests, helium pycnometry, and thin section petrography. The NYT is a well-studied rock, not
220 least because of its extensive use as a building stone in the Naples area. Typical of ignimbrite, it is
221 spatially quite variable^{17,46,47}. The deposit is up to ~80 m thick, and includes lenses which can be lithic-
222 rich, pumice-rich, or accretionary lapilli-rich. The blocks used in this testing are relatively lithic poor, lack
223 accretionary lapilli, and are characterised as a massive lapilli tuff.

224 Deformation experiments were carried out using a conventional triaxial testing machine⁴⁸ at a confining
225 pressure of 1.5 MPa, simulating depths of 100 – 150 m. Cylindrical samples of 40 mm diameter and 100
226 mm length are encased in a rubber jacket fitted with ports for AE sensors. The jacket housing the 12 AE
227 sensors also serves to separate the sample from the confining medium (silicone oil). To permit adequate
228 control at low stress, conventional mechanical feedback was bypassed and instead a constant flow rate
229 to the top piston/intensifier was used to ensure application of constant strain rate to the sample.

230 A digital logging system captured continuous signal data from all 12 AE sensors during the experiment at
231 10 MHz. These are first pre-amplified by 60dB, and passed through a hardware 1MHz low-pass filter.
232 These data were subsequently harvested using a 50 mV threshold to identify individual events for
233 spectral analysis.

234 Two different strain rates were tested; 1×10^{-5} , and $4 \times 10^{-6} \text{ s}^{-1}$, in an attempt to explore any strain
235 dependent control of the spectral characteristics of any AE. These values were chosen based on the
236 International Society for Rock Mechanics recommend strain rates in the order of 10^{-5} for simple
237 unconfined compressive strength testing of rock samples to brittle failure, and 10^{-6} for complete stress-
238 strain curves⁴⁹. This ensures that this work is both comparable to other tests in the literature, and
239 explores an order of magnitude strain rate variation.

240 X-ray Computed Tomography was carried out using a Zeiss Versa 510 X-ray microscope, achieving voxel
241 resolutions within the samples of 20 μm . The cores were imaged both before and after the deformation
242 experiments. The tomographic models were first viewed in an imaging software, and examined for
243 damage. For direct comparison (e.g. Figure 1) a random slice was selected from the middle portion of
244 the core in the pre-test tomographic model. Key identifying features were mapped, and then located in
245 the post-experiment tomographic model. The model was manipulated until a virtual slice matching the
246 same location in the pre-test was found in the post-test image.

247 **Acknowledgements**

248 We are grateful to Emily Butcher for sample preparation work, and to Emily Pegge for collating event
249 classifications.

250 **Competing Interests**

251 The authors declare no competing interests.

252 **Author Contributions**

253 PR drafted the paper. PR & PB carried out the laboratory experiments. PR, PB, and CB discussed results,
254 carried out analysis, and edited the draft paper.

255 **References**

- 256 1. Scarpa, R., Tilling, R. I. & McNutt, S. R. Seismic Monitoring and Eruption Forecasting of Volcanoes:
257 A Review of the State-of-the-Art and Case Histories. in *Monitoring and Mitigation of Volcano*
258 *Hazards* (1996). doi:10.1007/978-3-642-80087-0_3.
- 259 2. Chouet, B. A. Long-period volcano seismicity: Its source and use in eruption forecasting. *Nature*
260 (1996) doi:10.1038/380309a0.
- 261 3. Kilburn, C. R. J. Multiscale fracturing as a key to forecasting volcanic eruptions. *J. Volcanol.*
262 *Geotherm. Res.* **125**, 271–289 (2003).
- 263 4. Cortés, G. *et al.* Parallel System Architecture (PSA): An efficient approach for automatic
264 recognition of volcano-seismic events. *J. Volcanol. Geotherm. Res.* **271**, 1–10 (2014).
- 265 5. Benson, P., Vinciguerra, S., Nasser, M. H. B. & Young, R. P. Transition of low-frequency to very-
266 low frequency volcano seismicity : New experimental insights. (2008).
- 267 6. Lokmer, I., Saccorotti, G., Di Lieto, B. & Bean, C. J. Temporal evolution of long-period seismicity at
268 Etna Volcano, Italy, and its relationships with the 2004–2005 eruption. *Earth Planet. Sci. Lett.* **266**,
269 205–220 (2008).
- 270 7. McNutt, S. R. Seismic Monitoring and Eruption Forecasting of Volcanoes: A Review of the State-
271 of-the-Art and Case Histories. in *Monitoring and Mitigation of Volcano Hazards* (eds. Scarpa, R.,
272 Tilling, R. I. & McNutt, S. R.) 99–146 (Springer, 1996). doi:10.1007/978-3-642-80087-0_3.
- 273 8. Harrington, R. M. & Benson, P. M. Analysis of laboratory simulations of volcanic hybrid
274 earthquakes using empirical Green’s functions. *J. Geophys. Res. Solid Earth* **116**, 1–13 (2011).
- 275 9. Barberi, F., Corrado, G., Innocenti, F. & Luongo, G. Phlegraean Fields 1982–1984: Brief chronicle
276 of a volcano emergency in a densely populated area. *Bull. Volcanol.* (1984)
277 doi:10.1007/BF01961547.
- 278 10. Armienti, P., Barberi, F. & Innocenti, F. A model of the Phlegraean Fields magma chamber in the
279 last 10,500 years. *Bull. Volcanol.* (1984) doi:10.1007/BF01961566.
- 280 11. Scarpa, R., Tilling, R. I., Barberi, F. & Carapezza, M. L. The Problem of Volcanic Unrest: The Campi
281 Flegrei Case History. in *Monitoring and Mitigation of Volcano Hazards* 771–786 (Springer Berlin
282 Heidelberg, 1996). doi:10.1007/978-3-642-80087-0_23.
- 283 12. Hicks, A. & Few, R. Trajectories of social vulnerability during the Soufrière Hills volcanic crisis. *J.*
284 *Appl. Volcanol.* **4**, 10 (2015).
- 285 13. Kilburn, C. R. J., De Natale, G. & Carlino, S. Progressive approach to eruption at Campi Flegrei
286 caldera in southern Italy. *Nat. Commun.* **8**, 1–8 (2017).
- 287 14. Brown, S. K., Sparks, R. S. J. & Jenkins, S. F. Global distribution of volcanic threat. in *Global*
288 *Volcanic Hazards and Risk* (eds. Loughlin, S. C., Sparks, S., Brown, S. K., Jenkins, S. F. & Vye-
289 Brown, C.) 359–369 (Cambridge University Press, 2015). doi:10.1017/CBO9781316276273.025.
- 290 15. De Natale, G., Pingue, F., Allard, P. & Zollo, A. Geophysical and geochemical modelling of the
291 1982–1984 unrest phenomena at Campi Flegrei caldera (southern Italy). *J. Volcanol. Geotherm.*
292 *Res.* **48**, 199–222 (1991).

- 293 16. De Siena, L. *et al.* Source and dynamics of a volcanic caldera unrest: Campi Flegrei, 1983-84. *Sci.*
294 *Rep.* **7**, 1–13 (2017).
- 295 17. Orsi, G., D’Antonio, M., Vita, S. de & Gallo, G. The Neapolitan Yellow Tuff, a large-magnitude
296 trachytic phreatoplinian eruption: eruptive dynamics, magma withdrawal and caldera collapse. *J.*
297 *Volcanol. Geotherm. Res.* **53**, 275–287 (1992).
- 298 18. Deino, A. L., Orsi, G., de Vita, S. & Piochi, M. The age of the Neapolitan Yellow Tuff caldera-
299 forming eruption (Campi Flegrei caldera – Italy) assessed by ⁴⁰Ar/³⁹Ar dating method. *J.*
300 *Volcanol. Geotherm. Res.* **133**, 157–170 (2004).
- 301 19. Dvorak, J. J. & Berrino, G. Recent ground movement and seismic activity in Campi Flegrei,
302 southern Italy: episodic growth of a resurgent dome. *J. Geophys. Res.* (1991)
303 doi:10.1029/90JB02225.
- 304 20. Orsi, G., De Vita, S. & di Vito, M. The restless, resurgent Campi Flegrei nested caldera (Italy):
305 constraints on its evolution and configuration. *J. Volcanol. Geotherm. Res.* **74**, 179–214 (1996).
- 306 21. De Natale, G. *et al.* The Campi Flegrei caldera: unrest mechanisms and hazards. *Geol. Soc.*
307 *London, Spec. Publ.* **269**, 25–45 (2006).
- 308 22. Langella, A. *et al.* The Neapolitan Yellow Tuff: An outstanding example of heterogeneity. *Constr.*
309 *Build. Mater.* (2017) doi:10.1016/j.conbuildmat.2017.01.053.
- 310 23. Moon, V. G. Geotechnical characteristics of ignimbrite: A soft pyroclastic rock type. *Eng. Geol.* **35**,
311 33–48 (1993).
- 312 24. Quane, S. L. & Russell, J. K. Rock strength as a metric of welding intensity in pyroclastic deposits.
313 *Eur. J. Mineral.* **15**, 855–864 (2003).
- 314 25. Binal, A. Prediction of mechanical properties of non-welded and moderately welded ignimbrite
315 using physical properties, ultrasonic pulse velocity, and point load index tests. *Q. J. Eng. Geol.*
316 *Hydrogeol.* **42**, 107–122 (2009).
- 317 26. Fazio, M., Alparone, S., Benson, P. M., Cannata, A. & Vinciguerra, S. Genesis and mechanisms
318 controlling tornillo seismo-volcanic events in volcanic areas. *Sci. Rep.* **9**, 1–11 (2019).
- 319 27. Kendrick, J. E. *et al.* Tracking the permeable porous network during strain-dependent magmatic
320 flow. *J. Volcanol. Geotherm. Res.* **260**, 117–126 (2013).
- 321 28. Burlini, L. *et al.* Seismicity preceding volcanic eruptions: New experimental insights. *Geology* **35**,
322 183–186 (2007).
- 323 29. Main, I. Earthquake scaling. *Nature* vol. 357 27–28 (1992).
- 324 30. Hatton, C. G., Main, I. G. & Meredith, P. G. A comparison of seismic and structural measurements
325 of scaling exponents during tensile subcritical crack growth. *J. Struct. Geol.* **15**, 1485–1495 (1993).
- 326 31. Aki, K. & Koyanagi, R. Deep volcanic tremor and magma ascent mechanism under Kilauea,
327 Hawaii. *J. Geophys. Res.* (1981) doi:10.1029/JB086iB08p07095.
- 328 32. Burlini, L. *et al.* Seismicity preceding volcanic eruptions: New experimental insights. *Geology* **35**,
329 183–186 (2007).
- 330 33. Benson, P. M., Thompson, B. D., Meredith, P. G., Vinciguerra, S. & Young, R. P. Imaging slow

- 331 failure in triaxially deformed Etna basalt using 3D acoustic-emission location and X-ray computed
332 tomography. *Geophys. Res. Lett.* **34**, 1–5 (2007).
- 333 34. Fazio, M., Benson, P. M. & Vinciguerra, S. On the generation mechanisms of fluid-driven seismic
334 signals related to volcano-tectonics. *Geophys. Res. Lett.* **44**, 734–742 (2017).
- 335 35. Heap, M. J. *et al.* The influence of water on the strength of Neapolitan Yellow Tuff, the most
336 widely used building stone in Naples (Italy). *Bull. Volcanol.* (2018) doi:10.1007/s00445-018-1225-
337 1.
- 338 36. Townend, E. *et al.* Imaging compaction band propagation in Diemelstadt sandstone using
339 acoustic emission locations. *Geophys. Res. Lett.* **35**, 1–5 (2008).
- 340 37. Smith, R., Sammonds, P. R. & Kilburn, C. R. J. Fracturing of volcanic systems: Experimental insights
341 into pre-eruptive conditions. *Earth Planet. Sci. Lett.* **280**, 211–219 (2009).
- 342 38. Lockner, D. A., Byerlee, J. D., Kuksenko, V., Ponomarev, A. & Sidorin, A. Quasi-static fault growth
343 and shear fracture energy in granite. *Nature* **350**, 39–42 (1991).
- 344 39. Thompson, B. D. Observations of premonitory acoustic emission and slip nucleation during a stick
345 slip experiment in smooth faulted Westerly granite. *Geophys. Res. Lett.* **32**, L10304 (2005).
- 346 40. Harnett, C. E., Benson, P. M., Rowley, P. & Fazio, M. Fracture and damage localization in volcanic
347 edifice rocks from El Hierro, Stromboli and Tenerife. *Sci. Rep.* **8**, 1942 (2018).
- 348 41. Benson, P. M., Vinciguerra, S., Meredith, P. G. & Young, R. P. Spatio-temporal evolution of
349 volcano seismicity: A laboratory study. *Earth Planet. Sci. Lett.* **297**, 315–323 (2010).
- 350 42. Clarke, J. *et al.* The relation between viscosity and acoustic emissions as a laboratory analogue for
351 volcano seismicity. *Geology* **47**, 499–503 (2019).
- 352 43. Bean, C. J. *et al.* Long-period seismicity in the shallow volcanic edifice formed from slow-rupture
353 earthquakes. *Nat. Geosci.* **7**, 71–75 (2014).
- 354 44. Neuberg, J., Luckett, R., Baptie, B. & Olsen, K. Models of tremor and low-frequency earthquake
355 swarms on Montserrat. *J. Volcanol. Geotherm. Res.* **101**, 83–104 (2000).
- 356 45. Massonnet, D. & Feigl, K. L. Radar interferometry and its application to changes in the earth's
357 surface. *Rev. Geophys.* **36**, 441–500 (1998).
- 358 46. Barberi, F. *et al.* The campanian ignimbrite: a major prehistoric eruption in the Neapolitan area
359 (Italy). *Bull. Volcanol.* (1978) doi:10.1007/BF02597680.
- 360 47. Scarpati, C., Cole, P. & Perrotta, A. The Neapolitan Yellow Tuff ? A large volume multiphase
361 eruption from Campi Flegrei, Southern Italy. *Bull. Volcanol.* **55**, 343–356 (1993).
- 362 48. Benson, P. M. *et al.* Laboratory simulations of fluid-induced seismicity, hydraulic fracture, and
363 fluid flow. *Geomech. Energy Environ.* 100169 (2020) doi:10.1016/j.gete.2019.100169.
- 364 49. Fairhurst, C. E. ; Hudson, J. A. Draft ISRM suggested method for the complete stress-strain curve
365 for intact rock in uniaxial compression. *Int. J. Rock Mech. Min. Sci.* **36**, 279–289 (1999).